ARTICLE   OPEN

Check for updates

Restructured single parabolic band model for quick analysis in thermoelectricity

Jianbo Zhu [1], Xuemei Zhang[2,3], Muchun Guo[1], Jingyu Li[2], Jinsuo Hu[1], Songting Cai [4✉], Wei Cai[1], Yongsheng Zhang [2✉] and Jiehe Sui [1✉]

The single parabolic band (SPB) model has been widely used to preliminarily elucidate inherent transport behaviors of thermoelectric (TE) materials, such as their band structure and electronic thermal conductivity, etc. However, in the SPB calculation, it is necessary to determine some intermediate variables, such as Fermi level or the complex Fermi-Dirac integrals. In this work, we establish a direct carrier-concentration-dependent restructured SPB model, which eliminates Fermi-Dirac integrals and Fermi level calculation and emerges stronger visibility and usability in experiments. We have verified the reliability of such restructured model with 490 groups of experimental data from state-of-the-art TE materials and the relative error is less than 2%. Moreover, carrier effective mass, intrinsic carrier mobility and optimal carrier concentration of these materials are systematically investigated. We believe that our work can provide more convenience and accuracy for thermoelectric data analysis as well as instructive understanding on future optimization design.

INTRODUCTION

Thermoelectric (TE) materials can enable reversible conversion between electrical and thermal energy via strong electrical-thermal coupling effect, thus have enormous potential in waste heat power generation and refrigeration[1,2]. The conversion efficiency of TE materials is determined by the dimensionless figure-of-merit $ZT = S^2\sigma T/(\kappa_e + \kappa_L)$, where S, σ, T, κ_e, and κ_L are Seebeck coefficient, electrical conductivity, absolute temperature, electronic and lattice thermal conductivity, respectively[3]. Furthermore, the power factor is defined as $PF = S^2\sigma = S^2nq\mu$, a vital criterion for the output power density, wherein n is the carrier concentration, q the electronic charge, and μ the carrier mobility[4–6]. In practice, there are inevitable contradictions among these properties such as the opposite trend between the electrical conductivity and the Seebeck coefficient with increased carrier concentration[7–10]. Such conflicts notoriously impede further improvement of thermoelectric performance, and thereby raises the interest of excavating intrinsic independent parameters to optimize the thermoelectric property[11–15].

The Boltzmann transport equation can simulate the electrical transport properties of carriers in real crystals, and constitute a viable mean to investigate inherent material properties[16–18]. However, strictly solving this equation is computationally expensive in real materials systems, especially the ones with complex band structure and multiple scattering mechanisms. Therefore, some simplified models are proposed[19–22]. In particular, the derived single parabolic band (SPB) model is under the assumption that there is only one purely parabolic band contributing to the electronic conduction, and the acoustic phonon scattering is dominant in the system. This model has been commonly used to analyze fundamental thermoelectric characteristics for a long time[21,23,24]. In the SPB model, all transport properties can be established by four isolated key factors[25]: (i) Fermi level E_F (or reduced Fermi level $\eta = E_F/k_BT$), which reflects the doping level, (ii)

the effective mass m^*, which estimates the band dispersion, (iii) the scattering factor λ, which represents the mechanism of carrier scattering, and (iv) the relaxation time τ, which reflects the scattering intensity. One can obtain these important parameters from fitting the experimental transport measurements or from the density-functional theory (DFT) calculations. With these evaluated parameters, we can predict the TE performance. Comparing to both computationally expensive first principles calculations or directly solving the complex Boltzmann transport calculations, the simplicity of SPB model makes it a much more viable method to be used in practice. Therefore, the SPB model can realize a two-way analysis between theoretical and experimental data, from which we can quickly reveal the underlying physical mechanism that is not easy to obtain from the experimentally measured data[26–29], or reversibly realize designs of the electronic structure or screen potential TE materials by high throughput computational methods[30–33].

With the proliferation of SPB model applications, it is found that all properties are delicately governed by the reduced Fermi level and Fermi-Dirac integrals, which are defined as $F_n(\eta) = \int_0^{+\infty} x^n/(1 + e^{x-\eta})dx$, see Table 1 for more details. Due to the difficulty in analyzing and comprehending the integral, it is not easy to perform the SPB model based on experimental measurements. Thus, a simpler formula is needed practically[34–36]. If the Fermi level is within the band gap like intrinsic semiconductors, the η is far less than 0 ($E_F \ll -k_BT$), the Fermi-Dirac integral could be replaced by Eq. (1) under non-degenerate approximation (NDA)[25]

$$F_n(\eta) = \exp(\eta)\Gamma(n + 1), \tag{1}$$

where $\Gamma(n)$ is called the gamma function. On the other hand, if the Fermi level is deep in conduction/valence band like metals, the η is much greater than 0 ($E_F \gg k_BT$), and the Fermi-Dirac integrals can be expressed as Eq. (2) under the degenerate

[1]National Key Laboratory for Precision Hot Processing of Metals, Harbin Institute of Technology, Harbin, China. [2]Key Laboratory of Materials Physics, Institute of Solid State Physics, Chinese Academy of Sciences, Hefei, China. [3]Science Island Branch of Graduate School, University of Science and Technology of China, Hefei, China. [4]Department of Materials Science and Engineering, Northwestern University, Evanston, IL, USA. ✉email: songtingcainu@gmail.com; yshzhang@theory.issp.ac.cn; suijiehe@hit.edu.cn

Table 1. Key transport parameters modeled by SPB model and the corresponding dimensionless expressions.

Item	Modeled by SPB	Constant part	Dimensionless part
$n = n_0 n_r$	$\frac{(2m^* k_B T)^{3/2}}{2\pi^2 \hbar^3} \cdot F_{1/2}(\eta)$	$n_0 = 2.5094 \times 10^{19} \left(\frac{m^*}{m_e} \frac{T/K}{300}\right)^{3/2} \mathrm{cm}^{-3}$	$n_r = \frac{2}{\sqrt{\pi}} F_{1/2}(\eta)$
$S = S_0 S_r$	$\frac{k_B}{q}\left(\frac{2F_1(\eta)}{F_0(\eta)} - \eta\right)$	$S_0 = 86.1733\, \mu V/K$	$S_r = \frac{2F_1(\eta)}{F_0(\eta)} - \eta$
$\mu = \mu_0 \mu_r$	$\frac{4\pi \hbar^4 q C_1}{m_I^* \left(2m_b^* k_B T\right)^{3/2} \Xi^2} \cdot \frac{F_0(\eta)}{3F_{1/2}(\eta)}$	μ_0	$\mu_r = \frac{\sqrt{\pi}}{2} \frac{F_0(\eta)}{F_{1/2}(\eta)}$
$L = L_0 L_r$	$\left(\frac{k_B}{q}\right)^2 \left[3\frac{F_2(\eta)}{F_0(\eta)} - 4\left(\frac{F_1(\eta)}{F_0(\eta)}\right)^2\right]$	$L_0 = 0.7426 \times 10^{-8}\, W\Omega/K^2$	$L_r = 3\frac{F_2(\eta)}{F_0(\eta)} - 4\left(\frac{F_1(\eta)}{F_0(\eta)}\right)^2$

approximation (DA)[25]

$$F_n(\eta) = \frac{\eta^{n+1}}{n+1} + n\eta^{n-1}\frac{\pi^2}{6} + n(n-1)(n-2)\eta^{n-3}\frac{7\pi^4}{360} + \dots . \quad (2)$$

Since the series converge rapidly, we often use the first two items to describe transport parameters in general[25]. These simplifications under NDA and DA make the SPB model an accessible way to conveniently estimate the inherent properties of intrinsic (lightly doped) and heavily-doped (metal-like) semiconductors, respectively. Some derived equations are widely used under these circumstances. For example, we can evaluate the scattering factor λ by $S = \frac{k}{q}\left(\lambda + \frac{5}{2} - \eta\right)$ under NDA[25] or estimate m^* by $S = \frac{8\pi^2 k_B^2}{3qh^2} m^* T \left(\frac{\pi}{3n}\right)^{2/3}$ under DA[37,38]. However, for high performance TE materials, both simplified approximations above would not work properly because ZT and PF always reach the maximum when η is close to zero, i.e., E_F is close to band edge (Supplementary Discussion). This unphysical feature will lead to a large error of estimation (over 30%) when applying NDA or DA approximation. Therefore, it is of great interest to build a more general, accurate and simpler SPB model for better usability.

Apart from Fermi-Dirac integral calculations, the location of Fermi level is also an impediment to perform the SPB model. With the increase of the carrier concentration n, σ will increase while S will decrease and an optimal concentration exists, at which power factor reaches the maximum. Therefore, the optimization of n via extrinsic doping or intrinsic defects tuning is one of the most effective strategies in improving TE performance[39]. As mentioned above, the Fermi level E_F reflects the doping level or carrier concentration of the system, which plays a vital role in the classical SPB model since it correlates to all transport parameters of interest. Although n can be directly measured experimentally based on the Hall effect, it is unfeasible to solve E_F from experimental n in the current SPB framework because the exact density-of-state effective mass is further required and solving the Fermi-Dirac integral is unavoidable (Supplementary Table 1). Therefore, it is desirable to bypass the Fermi level or η, and directly quantify the carrier concentration dependency on TE parameters, such as the Seebeck coefficient and carrier mobility.

In this work, we introduced a restructured SPB model, in which all thermoelectric parameters are directly associated with carrier concentration by simple analytic expressions with less than 2% relative error. We have collected 490 groups of experimental data of state-of-the-art TE materials (see overview of all samples in Supplementary Fig. 1) to verity the feasibility and reliability of the restructured SPB model. The model provides a platform for deeper understanding of the carrier transport features in TE materials, such as electron–electron scattering intensity and maximum power factor. Based on our restructured model, a series of practical formulas could be constructed easily, which allows us to reasonably evaluate effective mass, facilely estimate intrinsic carrier mobility, and immediately predict optimum doping concentration and corresponding power factor using experimental data. Moreover, benefiting from the extreme simplicity of the

calculations, all evaluation of key factors based on the experimental data could be accomplished in a simple MS Excel file.

RESULTS AND DISCUSSION
Restructured SPB model
For convenience and general applicability, we carried out a nondimensionalization operation in the present restructured model as listed in Table 1. For the restructured SPB model, we establish the relationship between n and the three key transport parameters, namely S, μ, and L, and the other parameters such as σ, PF, and $\kappa_e(=L\sigma T)$ can be further derived from them. Besides the consideration of accuracy, the following three crucial design principles are proposed to improve the usability of restructured model:

(I) Simplicity, which is the major motivation of this work.
(II) Availability of an explicit inverse function, which allows us to directly calculate key factors and establish the expression between any two parameters.
(III) Compatibility with the conventional NDA & DA, which can promise usability in a wide range of carrier concentration, even when η goes to infinity.

As such, we can build well-designed SPB model by a series of practical formulas (see "Methods" section for more details). The three key transport parameters are expressed as

$$S_r = \ln\left(1.075 + \frac{e^2}{n_r}\right), \quad (3)$$

$$\mu_r = \left(1 + \frac{n_r}{2}\right)^{-1/3}, \quad (4)$$

$$L_r = L_{min} + \frac{L_{max} - L_{min}}{\left[1 + (n_r/2\pi)^{-3/2}\right]^{3/2}}, \quad (5)$$

where $L_{min} = 2$ and $L_{max} = \pi^2/3$ are limit values when η goes to negative infinity and positive infinity, respectively. Finally, the entire formula of original SPB and restructured SPB model is listed in Supplementary Table 1. As shown in Fig. 1, our restructured model has a good fit on classical SPB model in the entire range of carrier concentration. Calculation errors of the key parameters are all less than 0.02 at optimal doping concentration (Supplementary Fig. 2), which provides a more reliable experimental data analysis compared to previous NDA or DA model. We further verified the restructured SPB model with 490 groups of collected experimental data from many state-of-art TE materials, including BiSbTe (BST), metal chalcogenides (IV-VI), skutterudites (SKD), Zintl phases (Zintl), half-Heusler compounds (HH), silicon-germanium alloys (GeSi), metal oxide (Oxide), and so on, details are listed in Supplementary Table 1. The effective mass, intrinsic mobility and weighted mobility of these experimental TE materials are calculated by the restructured model, and the relative errors are
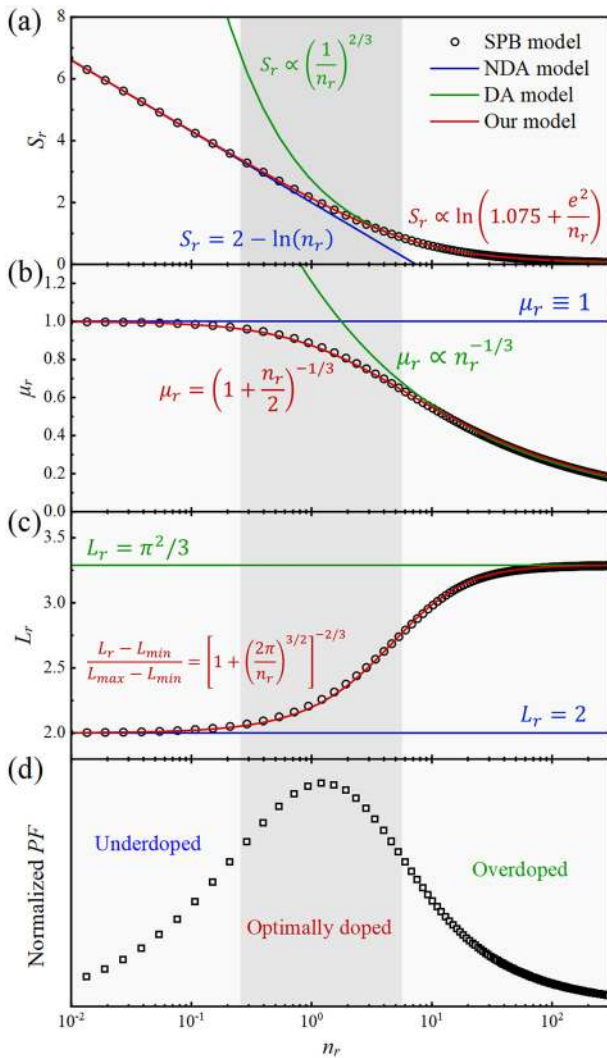
Fig. 1 **Reduced carrier concentration dependence on key transport parameters and power factor. a** Reduced Seebeck coefficient, **b** reduced mobility, **c** reduced Lorenz number and **d** normalized power factor. The open circles are generated by solving the classical SPB model, while solid lines are calculated by three simplified models, including the NDA model (blue), DA model (green) and our restructured model (red), respectively. The dark gray region represents the optimum range of reduced carrier concentration.

less than 2% (Supplementary Fig. 2). The computational cost of restructured SPB model is similar with NDA or DA model but the accuracy is greatly improved. Therefore, a quick analysis of experimental TE data can be implemented using the restructured SPB model, and the procedure to improve the TE performance will be accelerated.

Effective mass m^*

The effective mass m^*, sometimes called the Seebeck effective mass[40,41], is generally calculated by the relationship between Seebeck coefficient and carrier concentration, i.e., the Pisarenko plot. In fact, the m^* is an average density-of-state effective mass that reflects a general outline of the overall band edge. The configuration of band edge has a large influence on TE performance, for instance, increasing the number of carrier pockets at band edge can effectively increase m^* and results in a larger S. Therefore, developing a method by which m^* can be estimated both accurately and directly from experimental S and n

is of importance. Specifically, m^* is related to $n_0/n_{m,0}$ as shown in Table 1 and Eq. (6), where n_0 is the ratio of experimental n to n_r. In the classical SPB model, n_r is solved from Seebeck coefficient by a couple of Fermi-Dirac integrals[41], as listed in Table 1. Such process can be formalized as

$$\left(\frac{m^*}{m_e}\frac{T/K}{300}\right)^{3/2} = \frac{n_0}{n_{m,0}}, \tag{6}$$

$$n_0 = \frac{n}{n_r} = \frac{n}{S_r^{-1}(S/S_0)}, \tag{7}$$

wherein $S_r^{-1}(S/S_0)$ is the reverse function of $S_r(n_r)$, $n_{m,0}$ is a constant (2.5094×10^{19} cm^{-3}) and T is the absolute temperature in Kelvin (K). Based on Principle II, we can directly calculate n_r using Eq. (3) in our restructured model rather than solving Fermi-Dirac integrals as in the classical SPB model. Under NDA and DA, m^* can be calculate by[25]

$$\left(\frac{m^*}{m_e}\frac{T/K}{300}\right)^{3/2} = \frac{n}{n_{m,0}}\exp\left(\frac{S}{S_0} - 2\right), \tag{8}$$

$$\left(\frac{m^*}{m_e}\frac{T/K}{300}\right)^{3/2} = \frac{n}{n_{m,0}}\left(\frac{S}{\beta S_0}\right)^{3/2}. \tag{9}$$

While our model, m^* is expressed as,

$$\left(\frac{m^*}{m_e}\frac{T/K}{300}\right)^{3/2} = \frac{n}{n_{m,0}}\left[\exp\left(\frac{S}{S_0} - 2\right) - (1+\delta)\exp(-2)\right]. \tag{10}$$

When $\delta = 0.075$, it can be described as

$$\left(\frac{m^*}{m_e}\frac{T/K}{300}\right)^{3/2} = \frac{n}{n_{m,0}}\left[\exp\left(\frac{S}{S_0} - 2\right) - 0.1455\right]. \tag{11}$$

Four hundred and ninety groups experimental data are collected to verity the availability of NDA/DA model and our restructured model. Fig. 2 shows that the effective mass calculated by three simplified models (m^*_{cal}), including (a) NDA model, (b) DA model, and (c) our restructured SPB model, versus classical SPB model (m^*_η). Clearly, the calculated effective mass (m^*_{cal}) will be over-estimated and under-estimated in the NDA model and DA model as shown in Fig. 2a, b, respectively. In contrast, m^* calculated by our model shows a high consistency with the original SPB model with m^*_η spanning over two orders of magnitude as shown in Fig. 2c.

To further compare the accuracy of the calculated effective masses of different materials by these models, we plot m^*_{cal}/m^*_η with respect to their carrier concentration in Fig. 3. Consequently, if we adopt the Pisarenko relationship derived from the DA model (commonly expressed as $S = \frac{8\pi^2 k_B^2}{3qh^2}m^*T\left(\frac{\pi}{3n}\right)^{2/3}$) to calculate m^* among a series of samples with different dopant concentrations, we will gain a larger m^* in the ones with higher n even though the actual m^* is a constant, which gives misleading results. A similar situation exists in the NDA model. The degree of accuracy for these traditional models relies heavily on the carrier concentration: The NDA and DA models present reasonable results (m^*_{cal}/m^*_η converges to unity) at the extremely low and high concentrations (Fig. 3a), respectively. However, within the optimal carrier concentration range (10^{19} to 10^{21} cm^{-3}[39]) corresponding to the PF approaches maximum, both models have failed (Fig. 3b); the effective mass will be overestimated in NDA model but underestimated in DA model (a fraction of overestimated m^* in DA model are attributed to higher degree perturbed terms, see "Discussion" in SI). Specifically, at the optimally doping concentration range, the error is up to ~30%, which obviously would lead to significant problems in practice. In view of this, exploiting a model computing m^* well in a wide carrier concentration range is necessary to promise applicability for all sorts of TE materials.
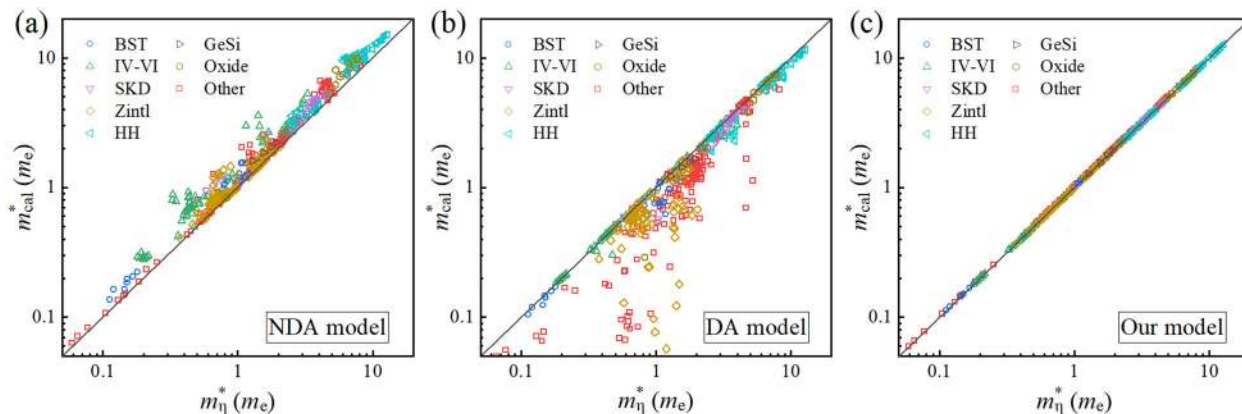
Fig. 2 Effective masses of different materials calculated by three simplified model (m^*_{cal}). **a** NDA model, **b** DA model and **c** our restructured model. m^*_η is the effective mass solved by the classical SPB model, and the solid line indicates $m^*_{cal} = m^*_\eta$.
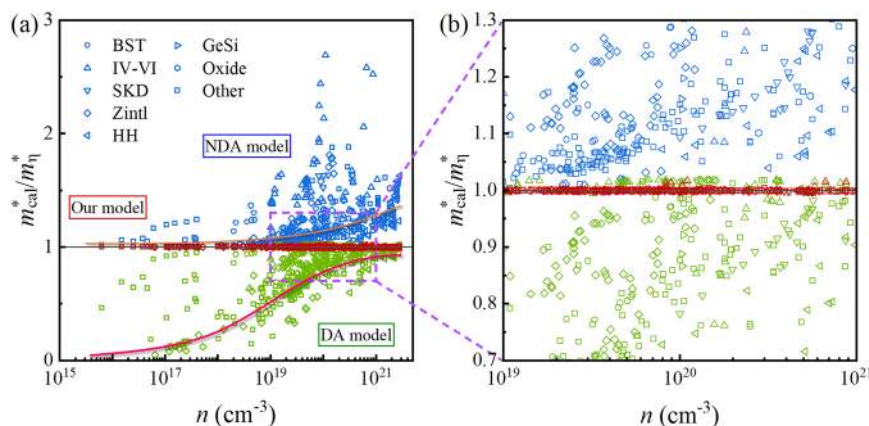

Fig. 3 The carrier concentration dependence on m^*_{cal}/m^*_η. **a** m^*_{cal}/m^*_η versus carrier concentration for our restructured model(red), NDA model (blue) and DA model (green). The orange and magenta solid lines are trend lines for NDA model and DA model, respectively. **b** Enlarged m^*_{cal}/m^*_η among 10^{19} cm^{-3} to 10^{21} cm^{-3}.

Arising from Principe III, our model successfully yields consistent results with m^*_η no matter how the carrier concentration is extremely low or high (Fig. 3). Thus, it convers not only the suitable carrier concentrations for the NDA and DA models, but also those cannot be described by the two models.

Intrinsic mobility μ_0

The actual mobility can be written as $\mu = \mu_0\mu_r$, where μ_r reflects the degradation brought by the electron interplay and μ_0 reflects the intrinsic scattering arising from the lattice. The parameter μ_0 is not highly dependent on carrier concentration, while the μ_r decreases with increased n[25]. For an intrinsic or lightly doped semiconductor, μ_r goes to unity and the experimentally measured μ approaches to μ_0. However, excellent thermoelectric materials are usually heavily-doped semiconductors and the electron interplay for carrier mobility cannot be neglected. In our restructured SPB model, the relationship between TE transport parameters and n is the main issue and the influence arising from carrier concentration is easy to evaluate. Here, the μ_r is facilely confirmed by Eq. (4) and μ_0 can be further estimated by

$$\mu_0 = \frac{\mu}{\mu_r} = \mu \cdot \left(1 + \frac{n}{2n_0}\right)^{1/3} \quad (12)$$

wherein $n_0 = \left(\frac{m^* T/K}{m_e \, 300}\right)^{3/2} \times 2.5094 \times 10^{19}$ cm^{-3} as listed in Table 1. m^* can be obtained by Eq. (11) using S and n, and Eq. (12) can also

be written as

$$\mu_0 = \mu \cdot \left[1 + \frac{S_r^{-1}(S/S_0)}{2}\right]^{1/3} = \mu \cdot \left[1 + \frac{1}{2\exp(S/S_0 - 2) - 0.2910}\right]^{1/3} \quad (13)$$

The freestanding μ_0 could easily be calculated from experimentally measured (μ, n) or (μ, S) using Eqs. (12) or (13) without any extra tedious calculations; this way, we can easily distinguish the contribution from μ_r and μ_0, which will help us understand the intrinsic scattering mechanism.

To visualize the impact of electron-electron scattering on the carrier mobility in TE materials, we plotted μ_r of collected TE materials in Fig. 4a. With the increase of carrier concentration, μ_r decreases from unity to half in some TE materials, which indicates that electron–electron scattering sometimes is comparable with the intrinsic scattering and cannot be simply ignored during analyses. Moreover, μ_r distribution shown in Fig. 4b reveals that μ_r mainly disperses at the range of 0.5–1. For a common case (±40 off the average), μ_r varies from 0.62 to 0.97, meaning that the fluctuation of μ_r referring to the average 0.81 is up to ±20% and μ_r cannot be regarded as a constant. Therefore, we conclude that Eq. (13) is effective to exclude the influence of inconstant electron–electron scattering on the experimental carrier mobility, and we can easily distinguish the intrinsic scattering originate from the lattice.
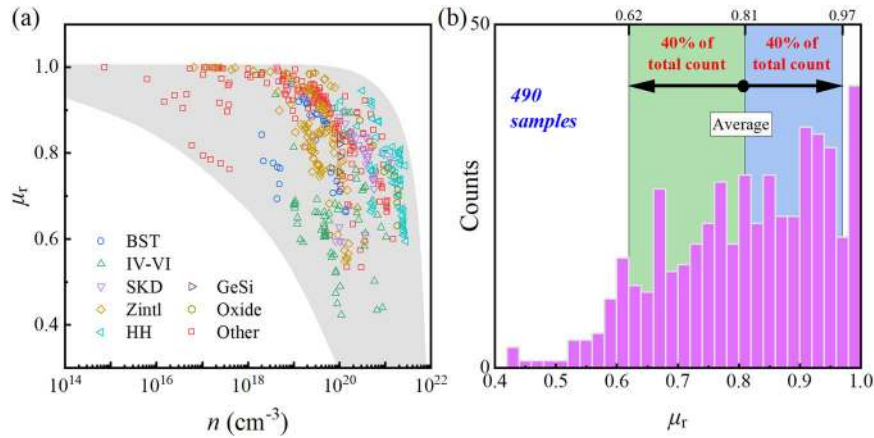
Fig. 4 Calculated reduced carrier mobility of all collected samples. a μ_r versus carrier concentration, **b** μ_r distribution. The gray region in **a** is to guide the eye, and the green region in **b** indicates a range below 40% of average μ_r and the blue area represents a range higher than 40% of average μ_r.

Weighted mobility μ_{WT}

The weighted mobility is an important combination parameter to evaluate the TE performance[41,42], and in most previous works it is defined as

$$\mu_w = \mu_0 \left(\frac{m^*}{m_e}\right)^{3/2}, \tag{14}$$

Since μ_w falls off with temperature as $T^{-3/2}$, in this work we include the absolute temperature weight to avoid such temperature-dependency with reference to Liu et al.'s work[43]. The weighted mobility is redefined as

$$\mu_{WT} = \mu_0 \left(\frac{m^*}{m_e}\frac{T/K}{300}\right)^{3/2}. \tag{15}$$

Here, 300 K is served as a reference temperature for convenience since most measurements are conducted at room temperature. In the classical SPB model, it can be concluded that the power factor at optimum n is determined via a rarely mentioned equation before,

$$PF_{opt} = 0.1212\mu_{WT}, \tag{16}$$

where PF_{opt} is in the unit of $\mu W\ cm^{-1}\ K^{-2}$ and μ_{WT} is in $cm^2\ V^{-1}\ s^{-1}$. Correspondingly, the optimum n is expressed as (see detail derivation in Supporting information)

$$n_{opt} = \left(\frac{m^*}{m_e}\frac{T/K}{300}\right)^{3/2} \times 3.15 \times 10^{19}\ cm^{-3} \tag{17}$$

or

$$n_{opt} = 1.26 \times n\left[\exp\left(\frac{S}{S_0} - 2\right) - 0.1455\right] \tag{18}$$

Combining the μ_0 calculated by Eq. (12) and m^* by Eq. (11), μ_{WT} and n_{opt} can be acquired directly without solving any complex equations. Additionally, Snyder et al recently proposed that the weighted mobility could be estimated by electrical conductivity and Seebeck coefficient if the Hall mobility measurement is absent.[44] This idea can also be expressed as Eq. (16) in our restructured model,

$$\mu_{WT} = \frac{\sigma}{n_{m,0}q}\frac{[1 + S_r^{-1}(S/S_0)/2]^{1/3}}{S_r^{-1}(S/S_0)} \tag{19}$$

It is verified that Eq. (16) is equivalent to the equation given by Snyder et al despite their differences in form (Supplementary Fig. 4), which further demonstrates the high flexibility of our model.

As mentioned above, Eqs. (16) and (17) can directly determine whether the doping level reaches optimum at any measuring temperature. To further verify, we collected the experimental data measured at not only room temperature but the ones at other temperature (Supplementary Table 3). Fig. 5a displays the experimental power factor (PF_{exp}) versus $\mu_{WT,cal}$ calculated by experimental S, n, and μ. We found that all data points are located on or below the solid line given by Eq. (16), which demonstrates that Eq. (16) provides the reasonable upper boundary of n-dependent power factor, i.e., the optimal power factor. Moreover, Fig. 5b is an illumination of the relationship depicted by Eq. (17), in which the size of symbol is positively related to the PF_{exp}. It is found that the closer to the solid line data point is, the higher power factor is obtained for most cases. Therefore, PF_{opt} and the corresponding n_{opt} carrier concentration can be immediately estimated by only one group of obtained transport parameters (S, n, and μ) in practice if the change of band scheme is negligible. This ability makes it easier to determine optimum doping concentration and explore potential TE materials.

Inspired by the decisive relationship between μ_{WT} and PF_{opt} given by Eq. (16), we can see that all kind of strategies benefiting to PF can be reflected in the change of μ_{WT}. In 1-2-2 type Zintl TE materials, the enhancement of power factor achieved by tailoring the band structure has drawn much attention recently[45–47]. Wang et al. adopted efficient dopant to shift the Fermi level deeper into the valence band so that all three band maxima can contribute to the TE transport (Fig. 6a) and corresponding power factor step from ~6 to ~9 cm² V⁻¹ s⁻¹ (150% increasing)[48]. Meanwhile, Zheng et al. alloyed $EuCd_2Sb_2$ with $EuZn_2Sb_2$, realizing a decrease in energy split between $p_{x,y}$ orbit and p_z orbit[49]. When x equals to 0.6 in $EuCd_{2-x}Zn_xSb_2$, the energy split disappears and a highest power factor is obtained as shown in Fig. 6b. In both examples above, μ_{WT} gives us a clear instruction on the change of intrinsic properties. Furthermore, the improvement of power factor in tin telluride (SnTe) also can be comprehended from the view of μ_{WT} as well as shown in Fig. 6c. If only tuning carrier concentration like a common case, such as Cu doping[50], the power factor is not desirable due to the large energy offset (~0.3 eV) between the light band and heavy hand[51]. Later, Zhang et al. demonstrated that a resonant level can be induced by In element, which corresponds to a drastic increase of μ_{WT} from ~100 to ~200 cm² V⁻¹ s⁻¹, and the power factor is enhanced to over 10 $\mu W\ cm^{-1}\ K^{-2}$[52]. Guo et al. employed In and Cu co-doping to improve the power factor up to 20 $\mu W\ cm^{-1}\ K^{-2}$, approaching the theoretical upper limit, which also reflects the increase of μ_{WT}[53]. Overall, comparing the experimentally measured power factors to the
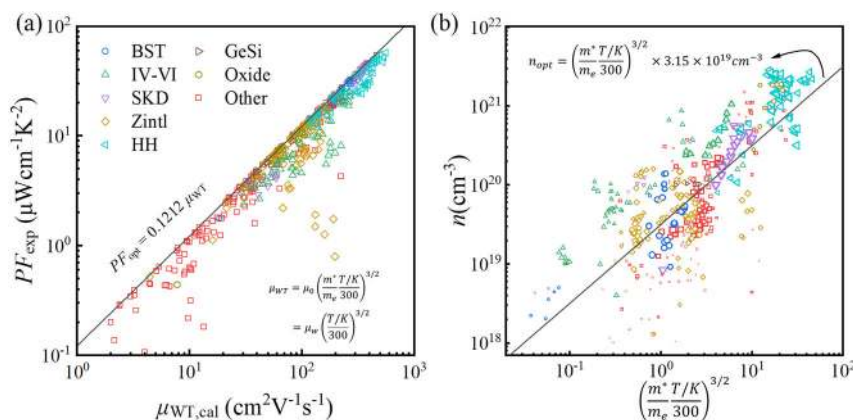
Fig. 5 Evaluations of maximum power factor and optimal carrier concentration. a Experimental power factor versus calculated weighed mobility. Data points close to the solid line indicate that they are optimally doped, while the ones off the line indicate under-doping or over-doping. **b** Carrier concentration versus calculated effective mass. The solid line denotes the optimum carrier concentration predicted by the SPB model and the size of symbols reflect the magnitudes of their corresponding power factors.
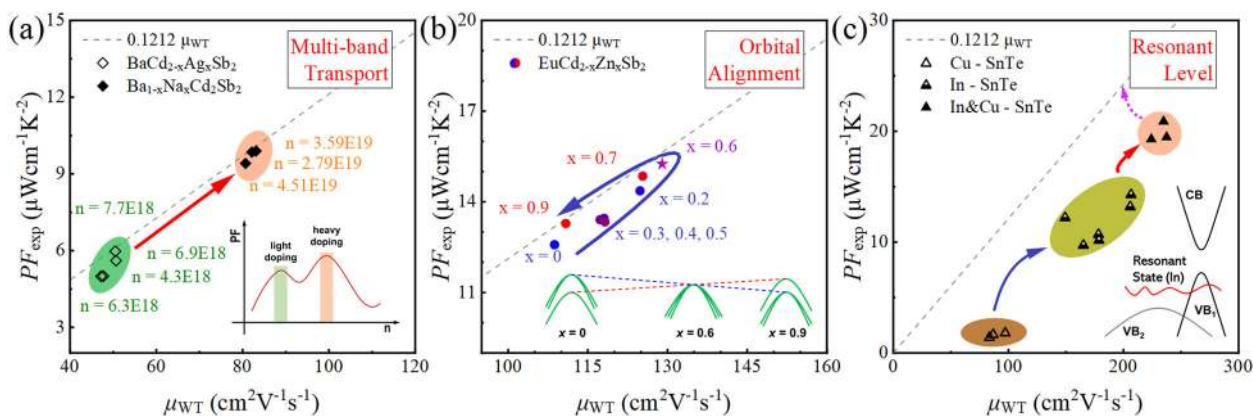
Fig. 6 Typical strategies of band engineering. a Multi-band transport[48], **b** orbital alignment[49] and **c** resonant level[50,52,53]. The dash line represents the upper limit of power factor predicted by our reconstructed SPB model (Eq. (16)).

optimal line given by Eq. (16) (Fig. 6), we notice that the power factors of doped $BaCd_2Sb_2$ and alloyed $EuCd_2Sb_2$-$EuZn_2Sb_2$ are almost reach their optimal values, and it is not too much space for further improvement. However, for the SnTe compound, there is still a gap between the experimental maximum power factor and theoretical upper limit, and thus more efforts are expected to improve the power factor.

In conclusion, our determined μ_{WT} is an intrinsic parameter that directly determines the upper limit of power factor, in which all the key factors are involved, including effective mass m^*, intrinsic mobility μ_0, and completely optimized doping level. μ_{WT} can be immediately evaluated from experimental transport parameter by our restructured SPB model, which provides essential information to further improve TE performance. Particularly, when the calculated electronic structures are absent in some doped semiconductor with complex unit cell, our restructured SPB model will supply more sufficient and more powerful evidence to assist band engineering analyzing.

Applicability of restructured SPB model

The collected 490 groups of experimental data on state-of-the-art TE materials verify the feasibility of our model and also give us an overview on their carrier transport characteristics. The effects of electron–electron scattering on carrier vary significantly in different TE materials, which can be neglected in lightly doped ones but is comparable with lattice scattering in heavily doped

ones, and an amendment is supplied as well. Moreover, a general evaluation of the optimal carrier concentration and corresponding optimal power factor is confirmed, which gives a clear physical picture about the carrier transport in TE materials. The achievement of maximum PF at optimal carrier concentration becomes possible using one group experimental data (including S, n, μ) at any carrier concentration, if the band scheme is not sensitive to dopant. In addition, our restructured model is still based on the single parabolic band mode; to perform an even wider range of applications in TE materials, we could further modify the model to include the multiband effects (a simple example including two conduction bands is given in Supplementary Discussion). By applying the restructured SPB model, we can reversibly understand the experimental transport data and the underlying physical properties, which will accelerate the procedure to improve the TE performance.

METHODS

Nondimensionalization

As listed in Table 1, all transport parameters in SPB model are expressed as a product of two parts: (1) the extracted constant part named as n_0, S_0, μ_0, L_0. Particularly, μ_0 here is a basic element and could be taken as the combination of the deformation potential Ξ, the elastic constants C_1, inertial effective mass m_I^* and band effective mass m_b^* under the SPB model[54]. (2) The dimensionless part named as n_r, S_r, μ_r, L_r; they only depend on reduced Fermi level and Fermi-Dirac integrals.

Design restructured model

Given their incompatibility of Principe II and Principe III we proposed above, we excluded some typical fitting models frequently used, such as polynomial and sigmoid function[35,44,55]. Since the Seebeck equations derived from NDA and DA model satisfies the Principe I and II well, we chose them as the initial formulas to derive the reconstructed model; some undetermined coefficients can be further assigned by fitting the primary data. Here we take the Seebeck equation in the restructured SPB as an example to demonstrate how the relationship between Seebeck coefficient and carrier concentration is derived.

In the NDA model, the reduced Seebeck coefficient S_r is related to the reduced carrier concentration n_r as

$$S_r = 2 - \ln(n_r) = \ln\left(\frac{e^2}{n_r}\right) \tag{20}$$

In the DA model,

$$S_r = \beta \cdot \left(\frac{1}{n_r}\right)^{2/3}, \beta = \frac{\pi}{3}\left(\frac{4\pi}{3}\right)^{2/3} \tag{21}$$

The Eqs. (20) and (21) are plotted with blue and green lines, respectively in Fig. 1a. Under Principe III, we reckon a general expression as

$$S_r = c_0 \cdot \left\{\ln\left[1 + \left(\frac{e^2}{n_r}\right)^{c_1}\right]\right\}^{c_2}, \tag{22}$$

where c_i ($i = 0, 1, 2$) are undetermined coefficients. When n_r goes to zero, i.e., $\eta \ll 0$,

$$\lim_{n_r \to 0} c_0 \cdot \left\{\ln\left[1 + \left(\frac{e^2}{n_r}\right)^{c_1}\right]\right\}^{c_2} = c_0 \cdot \left\{\ln\left[\left(\frac{e^2}{n_r}\right)^{c_1}\right]\right\}^{c_2} = c_0 \cdot \left\{c_1 \ln\left(\frac{e^2}{n_r}\right)\right\}^{c_2}, \tag{23}$$

which is compatible with Eq. (20) under NDA. When n_r goes to infinity, i.e., $\eta \gg 0$,

$$\lim_{n_r \to \infty} c_0 \cdot \left\{\ln\left[1 + \left(\frac{e^2}{n_r}\right)^{c_1}\right]\right\}^{c_2} = c_0 \cdot \left\{\left(\frac{e^2}{n_r}\right)^{c_1}\right\}^{c_2} = c_0 \cdot \left(\frac{e^2}{n_r}\right)^{c_1 \cdot c_2}, \tag{24}$$

which is compatible with Eq. (21) under DA. To further satisfy Principe I, we then simplify Eq. (22) as

$$S_r = \ln\left(1 + \delta + \frac{e^2}{n_r}\right), \tag{25}$$

wherein δ ($\delta \to 0$) is used to improve the goodness of fit when n_r is large. As n_r approaches zero, the parameter δ together with term "1" can be neglected and the Eq. (25) becomes equal to Eq. (20). In the end, when $\delta = 0.075$, Eq. (25) has a good fitting within 0.02 absolute error. For $\mu_r(n_r)$ and $L_r(n_r)$, similar processes are adopted to gain a good fitting result guided by above three principles we proposed.

DATA AVAILABILITY

The data that supports the findings of the work are in the manuscripts and Supplementary Information. Additional data will be available upon reasonable request.

CODE AVAILABILITY

We have made a Microsoft Excel Template (.xltx) file available for implementing the restructured SPB model at public GitHub repository (https://github.com/JianboHIT/rSPB).

REFERENCES

1. Liu, W., Jie, Q., Kim, H. S. & Ren, Z. Current progress and future challenges in thermoelectric power generation: from materials to devices. *Acta Mater.* **87**, 357–376 (2015).
2. Poudel, B. et al. High-thermoelectric performance of nanostructured bismuth antimony telluride bulk alloys. *Science* **320**, 634–638 (2008).
3. Snyder, G. J. & Toberer, E. S. Complex thermoelectric materials. *Nat. Mater.* **7**, 105–114 (2008).
4. Kim, H. S., Liu, W., Chen, G., Chu, C. & Ren, Z. Relationship between thermoelectric figure of merit and energy conversion efficiency. *Proc. Natl Acad. Sci. USA* **112**, 8205–8210 (2015).
5. Kim, H. S., Liu, W. & Ren, Z. Efficiency and output power of thermoelectric module by taking into account corrected Joule and Thomson heat. *J. Appl. Phys.* **118**, 115103 (2015).
6. Mehdizadeh Dehkordi, A., Zebarjadi, M., He, J. & Tritt, T. M. Thermoelectric power factor: enhancement mechanisms and strategies for higher performance thermoelectric materials. *Mater. Sci. Eng. R.* **97**, 1–22 (2015).
7. Zhu, H. et al. Discovery of TaFeSb-based half-Heuslers with high thermoelectric performance. *Nat. Commun.* **10**, 1–8 (2019).
8. Fu, C., Zhu, T., Liu, Y., Xie, H. & Zhao, X. Band engineering of high performance p-type FeNbSb based half-Heusler thermoelectric materials for figure of merit zT > 1. *Energy Environ. Sci.* **8**, 216–220 (2015).
9. Perumal, S., Roychowdhury, S., Negi, D. S., Datta, R. & Biswas, K. High thermoelectric performance and enhanced mechanical stability of p-type Ge1-xSbxTe. *Chem. Mater.* **27**, 7171–7178 (2015).
10. Cai, S. et al. Discordant nature of Cd in PbSe: off-centering and core-shell nanoscale CdSe precipitates lead to high thermoelectric performance. *Energy Environ. Sci.* **13**, 200–211 (2020).
11. Zhang, X. & Zhao, L. Thermoelectric materials: energy conversion between heat and electricity. *J. Materiomics* **1**, 92–105 (2015).
12. Park, J., Xia, Y., Ozolins, V. & Jain, A. Optimal band structure for thermoelectrics with realistic scattering and bands. *npj Comput. Mater.* **7**, 1–9 (2021).
13. Hao, S., Dravid, V. P., Kanatzidis, M. G. & Wolverton, C. Computational strategies for design and discovery of nanostructured thermoelectrics. *npj Comput. Mater.* **5**, 1–10 (2019).
14. Luo, Z. et al. Ultralow thermal conductivity and high-temperature thermoelectric performance in n-type K2.5Bi8.5Se14. *Chem. Mater.* **31**, 5943–5952 (2019).
15. Cai, S. et al. Ultralow thermal conductivity and thermoelectric properties of Rb2Bi8Se13. *Chem. Mater.* **32**, 3561–3569 (2020).
16. Madsen, G. K. H., Carrete, J. & Verstraete, M. J. BoltzTraP2, a program for interpolating band structures and calculating semi-classical transport coefficients. *Comput. Phys. Commun.* **231**, 140–145 (2018).
17. Li, X. et al. TransOpt. A code to solve electrical transport properties of semiconductors in constant electron–phonon coupling approximation. *Comput. Mater. Sci.* **186**, 110074 (2021).
18. Zhou, Z., Cao, G., Liu, J. & Liu, H. High-throughput prediction of the carrier relaxation time via data-driven descriptor. *npj Comput. Mater.* **6**, 1–6 (2020).
19. Hughes, A. C. & Buchan, A. G. A discontinuous and adaptive reduced order model for the angular discretization of the Boltzmann transport equation. *Int. J. Numer. Methods Eng.* **121**, 5647–5666 (2020).
20. Hong, M., Chen, Z. & Zou, J. Fundamental and progress of Bi2Te3-based thermoelectric materials. *Chin. Phys. B* **27**, 48403 (2018).
21. Naithani, H. & Dasgupta, T. Critical analysis of single band modeling of thermoelectric materials. *ACS Appl. Energy Mater.* **3**, 2200–2213 (2020).
22. Deng, T. et al. EPIC STAR: a reliable and efficient approach for phonon- and impurity-limited charge transport calculations. *npj Comput. Mater.* **6**, 1–11 (2020).
23. Zhou, T. et al. Thermoelectric properties of Zintl phase YbMg2Sb2. *Chem. Mater.* **32**, 776–784 (2020).
24. Fu, C. et al. Realizing high figure of merit in heavy-band p-type half-Heusler thermoelectric materials. *Nat. Commun.* **6**, 1–7 (2015).
25. Goldsmid, H. J. in *Introduction to Thermoelectricity* (ed. Goldsmid, H. J.) 25–44 (Springer, 2016).
26. Liu, Y. et al. Synergistically optimizing electrical and thermal transport properties of BiCuSeO via a dual-doping approach. *Adv. Energy Mater.* **6**, 1502423 (2016).
27. Liu, Z. et al. Lithium doping to enhance thermoelectric performance of MgAgSb with weak electron-phonon coupling. *Adv. Energy Mater.* **6**, 1502269 (2016).
28. Mao, J. et al. Manipulation of ionized impurity scattering for achieving high thermoelectric performance in n-type Mg3Sb2-based materials. *Proc. Natl Acad. Sci. USA* **114**, 10548–10553 (2017).
29. Zhang, J., Song, L. & Iversen, B. B. Insights into the design of thermoelectric Mg3Sb2 and its analogs by combining theory and experiment. *npj Comput. Mater.* **5**, 1–17 (2019).
30. Yan, J. et al. Material descriptors for predicting thermoelectric performance. *Energy Environ. Sci.* **8**, 983–994 (2015).
31. Malyi, O. I. & Zunger, A. False metals, real insulators, and degenerate gapped metals. *Appl. Phys. Rev.* **7**, 41310 (2020).
32. Recatala-Gomez, J., Suwardi, A., Nandhakumar, I., Abutaha, A. & Hippalgaonkar, K. Toward accelerated thermoelectric materials and process discovery. *ACS Appl. Energy Mater.* **3**, 2240–2257 (2020).
33. Bassman, L. et al. Active learning for accelerated design of layered materials. *npj Comput. Mater.* **4**, 1–9 (2018).
34. Kim, H., Gibbs, Z. M., Tang, Y., Wang, H. & Snyder, G. J. Characterization of Lorenz number with Seebeck coefficient measurement. *APL Mater.* **3**, 41506 (2015).

35. Fukushima, T. Precise and fast computation of generalized Fermi-Dirac integral by parameter polynomial approximation. *Appl. Math. Comput.* **270**, 802–807 (2015).

36. Chang, K. & Liu, C. An algorithm of calculating transport parameters of thermo-electric materials using single band model with optimized integration methods. *Comput. Phys. Commun.* **247**, 106875 (2020).

37. He, R. et al. Achieving high power factor and output power density in p-type half-Heuslers Nb1-xTixFeSb. *Proc. Natl Acad. Sci. USA* **113**, 13576–13581 (2016).

38. Bhardwaj, R. et al. Collective effect of Fe and Se to improve the thermoelectric performance of unfilled p-type CoSb3 skutterudites. *ACS Appl. Energy Mater.* **2**, 1067–1076 (2019).

39. Zhu, T. et al. Compromise and synergy in high-efficiency thermoelectric materials. *Adv. Mater.* **29**, 1605884 (2017).

40. Tang, Y. et al. Convergence of multi-valley bands as the electronic origin of high thermoelectric performance in CoSb3 skutterudites. *Nat. Mater.* **14**, 1223–1228 (2015).

41. Imasato, K., Kang, S. D., Ohno, S. & Snyder, G. J. Band engineering in Mg3Sb2 by alloying with Mg3Bi2for enhanced thermoelectric performance. *Mater. Horiz.* **5**, 59–64 (2018).

42. Qin, B., He, W. & Zhao, L. Estimation of the potential performance in p-type SnSe crystals through evaluating weighted mobility and effective mass. *J. Materiomics* **6**, 671–676 (2020).

43. Liu, W. et al. New insight into the material parameter B to understand the enhanced thermoelectric performance of Mg2Sn1-x-yGexSby. *Energy Environ. Sci.* **9**, 530–539 (2016).

44. Snyder, G. J. et al. Weighted mobility. *Adv. Mater.* **32**, 2001537 (2020).

45. Ovchinnikov, A. & Bobev, S. Zintl phases with group 15 elements and the transition metals: a brief overview of pnictides with diverse and complex structures. *J. Solid State Chem.* **270**, 346–359 (2019).

46. Zheng, L. et al. Ternary thermoelectric AB2C2 Zintls. *J. Alloy. Compd.* **821**, 153497 (2020).

47. Zhang, J. et al. Designing high-performance layered thermoelectric materials through orbital engineering. *Nat. Commun.* **7**, 1–7 (2016).

48. Wang, X. et al. Experimental revelation of multiband transport in heavily doped BaCd2Sb2 with promising thermoelectric performance. *Mater. Today Phys.* **8**, 123–127 (2019).

49. Zheng, L., Li, W., Wang, X. & Pei, Y. Alloying for orbital alignment enables thermoelectric enhancement of EuCd2Sb2. *J. Mater. Chem. A* **7**, 12773–12778 (2019).

50. Brebrick, R. F. & Strauss, A. J. Anomalous thermoelectric power as evidence for two-valence bands in SnTe. *Phys. Rev.* **131**, 104–110 (1963).

51. Chen, Z. et al. Routes for advancing SnTe thermoelectrics. *J. Mater. Chem. A* **8**, 16790–16813 (2020).

52. Zhang, Q. et al. High thermoelectric performance by resonant dopant indium in nanostructured SnTe. *Proc. Natl Acad. Sci. USA* **110**, 13261–13266 (2013).

53. Guo, F. et al. Simultaneous boost of power factor and figure-of-merit in In-Cu codoped SnTe. *Small* **15**, 1902493 (2019).

54. Bardeen, J. & Shockley, W. Deformation potentials and mobilities in non-polar crystals. *Phys. Rev.* **80**, 72–80 (1950).

55. Zhang, X. et al. Electronic quality factor for thermoelectrics. *Sci. Adv.* **6**, c726 (2020).

AUTHOR CONTRIBUTIONS

J.Z. and J.S. conceptualized the work, X.Z., J.L. and S.C. performed data analysis. J.H. and M.G. collected all experimental data. Y.Z. and W.C. supervises the progress of the entire work. All authors contributed to the discussions and analyses of the data, and approved the final version.

COMPETING INTERESTS

The authors declare no competing interests.

ADDITIONAL INFORMATION

Supplementary information The online version contains supplementary material available at https://doi.org/10.1038/s41524-021-00587-5.

Correspondence and requests for materials should be addressed to S.C., Y.Z. or J.S.

Reprints and permission information is available at http://www.nature.com/reprints

Publisher's note Springer Nature remains neutral with regard to jurisdictional claims in published maps and institutional affiliations.